

# Reducing strain fluctuations in quantum dot devices by gate-layer stacking

Collin C. D. Frink, Benjamin D. Woods, Merritt P. Losert, E. R. MacQuarrie, M. A. Eriksson, and Mark Friesen  
*Department of Physics, University of Wisconsin-Madison, Madison, Wisconsin 53706, USA*

Nanofabricated metal gate electrodes are commonly used to confine and control electrons in electrostatically defined quantum dots. However, these same gates impart a complicated strain pattern that affects the confinement potential and potentially impairs device functionality. Here we investigate strain-induced fluctuations of the potential energy in Si/SiGe heterostructures, caused by (i) lattice mismatch, (ii) materials-dependent thermal contraction, and (iii) depositional stress in the metal gates. By simulating different gate geometries, ranging from simple to realistically complicated, and including features like overlapping metal and oxide layers, we can explain most observed strain features. In particular, we show that strain-induced potential fluctuations can be suppressed by employing overlapping gates that cover the whole active region, when the oxide layers are thin. These results suggest that strain effects should not present a serious challenge to qubit uniformity when following simple design rules.

## I. INTRODUCTION

Gate-defined quantum dots in Si/SiGe quantum wells are a promising platform for large-scale quantum computation [1–3], where recent demonstrations of single and two qubit gates have exceeded error correction thresholds [4–6]. While these achievements represent important milestones, useful quantum hardware will require vast arrays of reliable, low-error qubits. Scaling up will require a level of qubit reproducibility and uniformity on par with transistors in modern integrated circuits [7, 8]. Such uniformity has been achieved for certain dot properties like orbital and charging energies [9], but remains a challenge for properties like the valley energy splitting [10], due to the inherent atomistic disorder of the SiGe random alloy [11, 12]. Some types of non-uniformity are potentially reconfigurable, such as interfacial trapped charge [13, 14], which can modify the local electrostatics [15] and cause the formation of unintentional quantum dots [16–18]. Other sources of variability (e.g., valley splitting) are immutable, and are prescribed during heterostructure growth or device fabrication.

Local strain fields can significantly affect the in-plane confinement potential of quantum dots [19, 20]. These strains arise from the structural or geometrical features of a device, such as metal electrodes or etched regions, which are intentionally patterned atop the quantum well that houses the qubits [21]. Such structures are carefully designed to provide electrostatic control of the qubit environment. However, the strains arising from these gates can have a very different effect on the confinement potential than the intended one, resulting in energy variations on the order of meV [22, 23], which is comparable to the electrostatic confinement. Such fluctuations can cause unintentional quantum dots [19], and can affect exchange interactions between electrons in neighboring dots [3, 24–26]. Despite such compelling arguments to treat the strain and electrostatics on equal footing, this is seldom done in experiments or simulations.

In this work, we numerically investigate strain effects arising from three main sources: (i) lattice mismatch be-

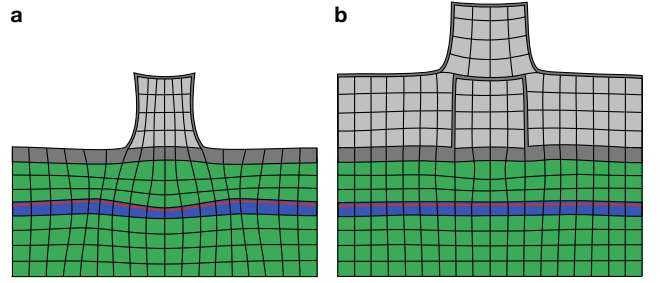


FIG. 1. Schematic illustration of the suppression of strain fluctuations by gate-layer stacking. **a** Non-uniform strain in a Si/SiGe quantum well (blue/green) is induced beneath a metal wire (light gray) upon cooling the device, due to differing thermal expansion coefficients in the materials. Red line indicates the plane of the two-dimensional electron gas (2DEG). **b** Same as **a**, with an additional metal wire or plane covering the original wire. If the oxide layer (dark gray) between the wires is sufficiently thin, the presence of the top wire suppresses the local strain fluctuations in the quantum well. In both diagrams, note that strains and structural deformations have been exaggerated for visual clarity; see simulations, below, for numerically accurate results.

tween the Si in the quantum well and the SiGe alloy of the barriers [27], (ii) unequal contractions of different materials as the device is cooled [19], and (iii) depositional stress, which occurs in a metal when it is deposited on a semiconductor or an oxide [28]. These strain calculations are used to estimate conduction-band energies in the Si quantum well, as explained in Methods, from which we deduce the locally varying confinement potential. (In Supplementary Fig. S3, we also include the corresponding electrostatic potential.) Beginning with simple gate structures, we work our way up to realistic devices measured in qubit experiments [29, 30]. Due to the long-range nature of the strain fields, our simulations exhibit both short-range variations that mirror the locally varying gate structure, as well as smoother, averaged behavior arising from multiple gates, which is manifested (for example) as edge effects.

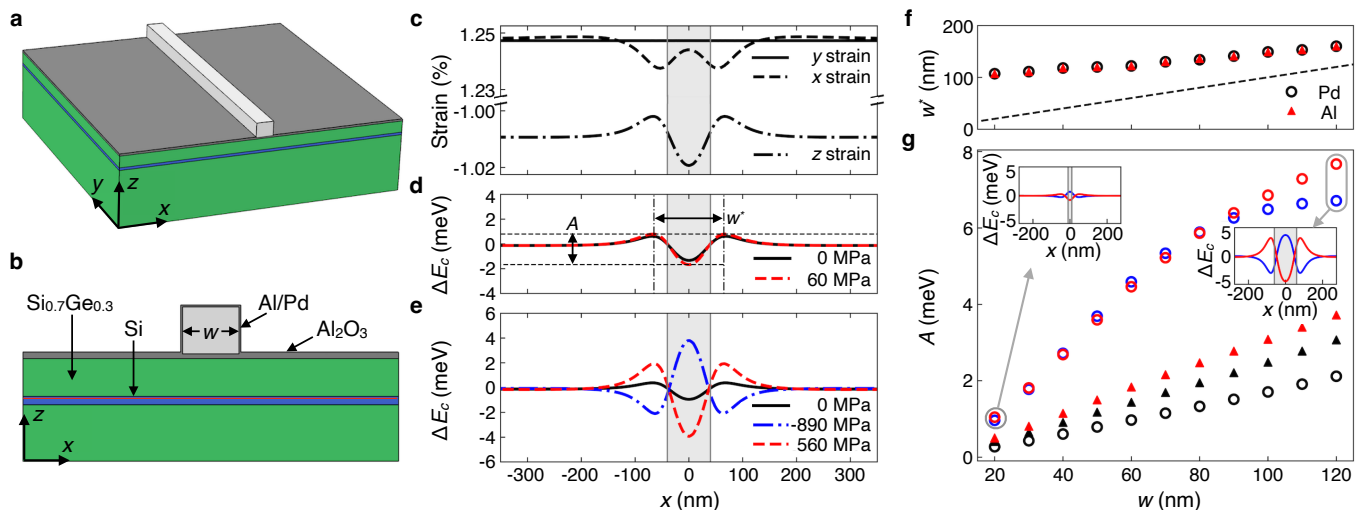


FIG. 2. Strain simulations of a single-wire geometry. **a,b** 3D and cross-sectional views, respectively. From bottom to top, the thicknesses of the  $\text{Si}_{0.7}\text{Ge}_{0.3}$  virtual substrate (green), Si quantum well (blue),  $\text{Si}_{0.7}\text{Ge}_{0.3}$  spacer (green), and insulating  $\text{Al}_2\text{O}_3$  layer (dark gray) are  $2\ \mu\text{m}$ ,  $9\ \text{nm}$ ,  $30\ \text{nm}$ , and  $10\ \text{nm}$ , respectively. A metal wire (light gray) of height  $60\ \text{nm}$  and variable width  $w$  is formed of Al or Pd. The wire is covered on the top and sides by a thin  $2\ \text{nm}$   $\text{Al}_2\text{O}_3$  layer (dark gray; not shown in **a**, for clarity). All strain and energy fluctuations in this work are evaluated on the horizontal red line in **b**, corresponding to the plane of the 2DEG, which is taken to lie  $1.5\ \text{nm}$  below the top quantum-well interface. **c** Diagonal strain components  $\varepsilon_{xx}$ ,  $\varepsilon_{yy}$ , and  $\varepsilon_{zz}$ . **d,e** Corresponding conduction-band energy offsets  $\Delta E_c$ , for Al (**d**) or Pd (**e**) wires of width  $w = 80\ \text{nm}$  (shaded region), with depositional strains as indicated. We also assume thermal contractions for a temperature of  $1\ \text{K}$ , as described in Methods. The peak-to-peak width  $w^*$  and amplitude  $A$  of the fluctuations are defined in **d**. **f,g** Results for  $w^*$  and  $A$  are plotted as a function of the actual wire width  $w$ . The dashed line in **f** corresponds to  $w^* = w$ . Closed triangles in **g** correspond to Al wires, following the color scheme in **d**, while open circles correspond to Pd, following the color scheme in **e**.

By exploring gate designs commonly used in experiments, we can draw some practical conclusions for designing future experiments. Most notably, we find that undesirable strain fluctuations can be greatly suppressed by tightly stacking multiple layers of gates. To illustrate this point, in Fig. 1a, we depict the strong, locally varying strain found in the plane of the quantum well, directly below an isolated, narrow gate. In contrast, it is clear that a wide gate will produce a relatively uniform strain in the quantum well below, except near the edges of the gate. Now if we consider several closely spaced gates, or an overlapping geometry like the one shown in Fig. 1b, the strain will be nearly uniform, similar to the situation for a wide gate. We note that this result cannot hold for a thick oxide layer, because the overlapping gate will be too far away to have an effect, resulting in a strain response more similar to Fig. 1a. We also observe more subtle behaviors from gate stacking, including a change of sign in the strain (for the cases of individual, overlapping gates vs a global gate), and the formation of a double-well (or double-barrier) feature on either side of a wire. In the following discussion, we elaborate on these and other phenomena, and provide additional numerical details.

## II. RESULTS

To study the physics of strain fluctuations under top gates, and particularly, the effect of gate-layer stacking, we simulate four systems of varying complexity. The first system consists of a long metal gate fabricated atop an otherwise uniform Si/SiGe heterostructure, as shown in Fig. 2, which serves as a minimal model for describing the effects of local strain. The second system considers the effects of several closely spaced gates, with or without a narrow crossing gate, as shown in Fig. 3. Figures 4 and 5 correspond to the experimental devices in Refs. [29] and [30], respectively. Here, the effects of gate-layer stacking are studied by including different subsets of overlapping gates in the simulations. Figure 5 also demonstrates the importance of oxide-layer thickness. All results shown here make use of the Solid Mechanics module of COMSOL Multiphysics [31], as described in Methods. The simulations incorporate all three sources of strain described above, with the materials parameters described in Methods. For the thermal contraction simulations, we assume the devices are cooled from  $T = 293.15$  to  $1\ \text{K}$ .

### A. Single wire

We first consider the simple wire geometry shown in Fig. 2a, where the wire is uniform along the  $\hat{y}$  direc-

tion. The corresponding cross section is shown in Fig. 2b. From bottom to top, the heterostructure in our simulations consists of a 2  $\mu\text{m}$  layer of strain-relaxed  $\text{Si}_{0.7}\text{Ge}_{0.3}$ , a 9 nm Si quantum well, another 30 nm spacer layer of  $\text{Si}_{0.7}\text{Ge}_{0.3}$ , and a 10 nm insulating layer of  $\text{Al}_2\text{O}_3$ . We assume that all interfaces in this structure are grown epitaxially, and that the quantum well is fully strained. The Si layer therefore experiences biaxial tensile strain due to the larger bulk lattice constant of SiGe. Except where noted (Fig. 5), we use this same heterostructure in all simulations reported below. Moreover the strain, and the energy variations it causes, are always evaluated in the plane of the two-dimensional electron gas (2DEG), which we take to lie 1.5 nm below the top quantum-well interface.

We first simulate just the heterostructure geometry, without any top gate. Here, the strain is caused by a combination of lattice mismatch and thermal contraction, giving the following diagonal strain results in the plane of the 2DEG:  $\varepsilon_{xx} = \varepsilon_{yy} = 1.248\%$  and  $\varepsilon_{zz} = -1.01\%$ . The strain causes an energy shift of the conduction band, as described in Methods, which accounts (in part) for the vertical confinement potential of the quantum well. We take as a reference point the conduction-band minimum at a point far away from the region of interest. Since the strain and the conduction-band minimum are both uniform in this geometry, the energy shift compared to the reference point,  $\Delta E_c$ , is zero across the whole sample.

For the wire geometry of Figs. 2a and 2b, we consider an Al metal wire formed directly atop the oxide layer as shown, with a fixed height of 60 nm and a variable width  $w$ . The wire causes local strain fluctuations, due to a combination of depositional stress and thermal contractions, with results shown in Fig. 2c. Here all three diagonal strain-tensor components are plotted ( $\varepsilon_{xx}$ ,  $\varepsilon_{yy}$ , and  $\varepsilon_{zz}$ ). The corresponding conduction-band energy shifts are shown in Fig. 2d, for cases with and without depositional stress, as indicated. Similarly, Fig. 2e shows results for a Pd wire. In this case, different values (and signs) of the depositional stress are reported in the literature; we therefore consider two different values, as well the case of no depositional stress. (The latter results differ from those in the Al wire because of the different thermal contractions.) For both sets of simulations, the energy shift converges to its asymptotic value far from the wire, such that  $\Delta E_c = 0$ . Near the gates,  $\Delta E_c$  has strong variations on the scale of several meV. For the Al wire, the depositional stress is low, and we see that its contribution to  $\Delta E_c$  is small. For the Pd wire, the opposite is true, and the depositional stress is seen to dominate over the thermal stress. Here,  $\Delta E_c$  changes sign for the case of depositional tensile stress (560 MPa) vs compressive stress (-890 MPa). Supplementary Fig. S1 provides further insight into the specific shape of the strain profiles.

The dependence of strain effects on wire width is shown in Figs. 2f and 2g. We now introduce two parameters to characterize the  $\Delta E_c$  variations, as defined in Fig. 2d: the peak-to-peak width  $w^*$  and the trough-to-peak ampli-

tude  $A$ . These two parameters are plotted in Figs. 2f and 2g, respectively. The width parameter  $w^*$  is found to be essentially universal, with no significant dependence on materials or strain parameters. Interestingly,  $w^*$  asymptotes to a nonzero value for small  $w$ , and to  $w + w_0$  (with  $w_0 > 0$ ), for large  $w$ . Both effects can be understood in terms of an approximate “45° rule,” in which the strain fields extend out at an angle from the gates, with details depending slightly on the wire width. We note that there is no contradiction that  $w^*$  remains nonzero as  $w \rightarrow 0$ , since  $A \rightarrow 0$  also in this limit. However, there is an interesting dependence of  $A$  on the strain parameters and on  $w$ . We see that  $A$  initially follows a linear dependence on  $w$  in all cases. For the case of the red and blue circle data, this behavior changes at around  $w \approx 80\text{-}90$  nm, where  $A$  begins to plateau as the two edges of the wire no longer affect each other’s local strain field. Such plateaus are generally expected for large  $w$ .

## B. Parallel wires

We now study how the single-wire picture is modified in the presence of additional wires, spaced closely enough that their strain fields overlap. We consider the geometries shown in Figs. 3a and 3b, comprising five parallel Al wires of width 80 nm and height 70 nm, with gaps of 40 nm between the wires, representing a typical gate pitch for quantum-dot qubits [29]. In addition to these five gates, the first device also includes a crossing gate with the same cross-section dimensions, oriented perpendicular to the wires and separated from those wires by a 2 nm insulating layer of  $\text{Al}_2\text{O}_3$ . The second device has a 100 nm gap in place of the crossing gate, but also includes a 2 nm conformal oxide layer covering the whole surface. All the wires in these simulations are taken to be very long, to suppress potential edge effects. The strains are computed, as described above, and the resulting conduction-band minima are plotted as a function of lateral position in Figs. 3c and 3d. Several cuts are taken in the plane of the 2DEG, along the indicated lines, yielding the results shown in Figs. 3e and 3f.

In these multigate devices,  $\Delta E_c$  exhibits short-range variations that mirror the local gate structure, and a slowly varying envelope arising from long-range strain fields.  $\Delta E_c$  differs in interesting ways for the two geometries, especially near the crossing regions ( $y \approx 0$ ). The trough-to-peak amplitudes are similar to those observed in Fig. 2, indicating that the short-range features are mainly governed by the gate structure right above the 2DEG. It is important to note that the amplitudes of these oscillations are large enough to produce unintentional dots. For example, the series of dips along the gray dashed line in Fig. 3d are 3 meV deep, compared to orbital excitation energies of 1-3 meV in typical dots. Such potential fluctuations are also large enough to affect exchange interactions, which are used to construct two-qubit gates. For example, it has been shown that a

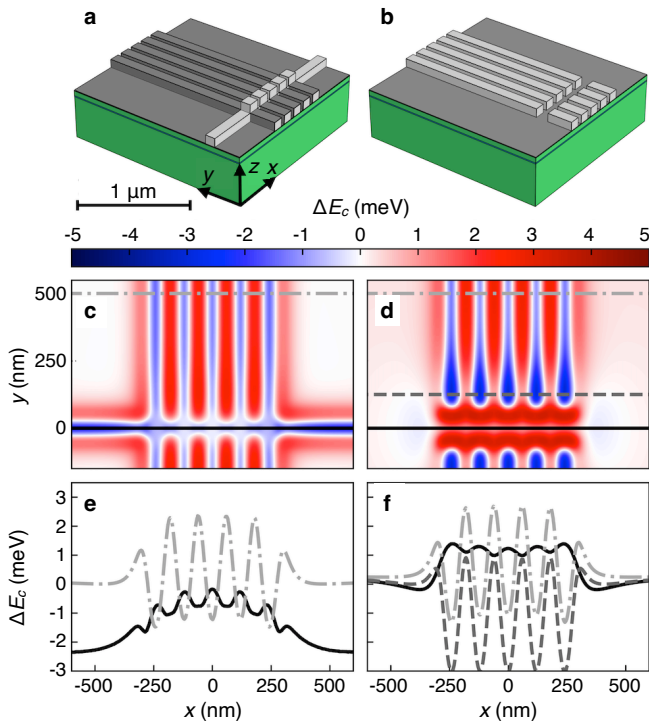


FIG. 3. Strain simulations of a parallel-wire geometry, with a crossing-wire or a gap at  $y = 0$ , fabricated on the same heterostructure as Fig. 2. **a** 3D view of five parallel Al wires (80 nm wide, 70 nm tall, with 40 nm gaps between them) with a perpendicular crossing wire of the same dimensions. Here, the lower set of gates is covered by a 2 nm layer of  $\text{Al}_2\text{O}_3$ , separating it from the crossing wire. **b** Same as **a**, except that the crossing wire is replaced by a gap of width 100 nm. In both **a** and **b**, the uppermost 2 nm oxide layer is not shown, for clarity. **c,d** Conduction-band energy modulations  $\Delta E_c$ , for the geometries shown in **a** and **b**, respectively. **e,f** Linecuts from **c** and **d**, respectively. We highlight an important result here, that the energy fluctuations are strongly suppressed below either the crossing wire (**c**) or the gap (**d**).

useful exchange interaction of strength  $J \approx 10$  MHz requires having a tunnel barrier between two Si/SiGe dots with a height less than 1 meV [3]. If necessary, such strain-induced variations could potentially be compensated electrostatically; however, for complicated gate geometries, the competition between short- and long-range strain features could make this challenging. A desirable approach is therefore to compensate some of the fluctuation through gate design, as discussed below. Finally, we note that the envelope of the potential variations can also vary by several meV, even across a series of identical wires. This is particularly evident in the dot-dashed linecuts of Figs. 3e and 3f, where the roughly 1 meV difference in  $\Delta E_c$  between neighboring wires can be viewed as an effective detuning shift between quantum dots.

We now study the effect of overlapping gates in Fig. 3e by comparing results directly underneath the crossing gate (solid line) to those far away from the gate (dot-

dashed line). While the envelopes of the two curves appear similar, the amplitudes of their short-range oscillations differ by a factor of six. Moreover, the oscillations are seen to have opposite sign.

One would like to understand and potentially predict such interesting behavior. Indeed, for simple geometries, with only a few materials layers (e.g., Fig. 2, or the dot-dashed line in Fig. 3c), this is often possible. However more-complicated geometries, particularly those with nontrivial three-dimensional (3D) features, can give rise to unexpected behavior, like the sign change of the short-range oscillations. In Methods, we note that  $\Delta E_c$  is dominated by the  $z$  component of the strain,  $\varepsilon_{zz}$ , which depends on multiple factors, including locally varying interface profiles, the specific values of thermal expansion coefficients, and the various layer thicknesses. In fact, in Sec. IID below, we study a geometry where simply changing the oxide thickness, keeping everything else fixed, causes a similar sign change in the short-range oscillations. Notwithstanding these challenges, we can make some general observations. For example, in Fig. 3e, the oscillations change sign, moving from the dot-dashed to solid linecuts, indicating that a different linecut, placed somewhere between these two lines, should provide more strongly suppressed oscillations. Similarly, modifying the gate geometry could also reduce the oscillation amplitude. For example, a narrower crossing gate, or more-closely spaced parallel gates could both produce the desired smoothing effect. These results demonstrate that gate-layer stacking can provide an effective strategy for reducing short-range strain variations.

An alternative scheme for suppressing short-range oscillations is simply to remove the top gates (solid line in Figs. 3d and 3f). In this case, the strain fields are mainly long-range, as desired; however, as a result, short-range electrostatic control is also sacrificed. While relatively smooth potentials can be achieved along the  $y = 0$  lines of both geometries in Fig. 3, we note that their qualitative behaviors differ. The dip features in  $\Delta E_c$  along the gray dashed line in Fig. 3f are especially prominent, indicating that edge effects (e.g., caused by the terminal ends of wires) have a particularly strong effect on both short- and long-range behaviors.

### C. Quadruple-quantum-dot device

We now consider gate-layer stacking in realistic and commonly used overlapping gate geometries, like the quadruple quantum dot shown in Fig. 4 [29]. For the simulations, we assume the same heterostructure as in Fig. 2 — now with three overlapping layers of Al metal gates. From bottom to top, these correspond to screening gates (maroon), plunger or reservoir gates (blue), and tunnel-barrier gates (yellow). We also include 2 nm  $\text{Al}_2\text{O}_3$  insulating layers between each of the metal layers. In the lower portion of the image, the plunger gates define four quantum dots and two 2DEG reservoirs, on

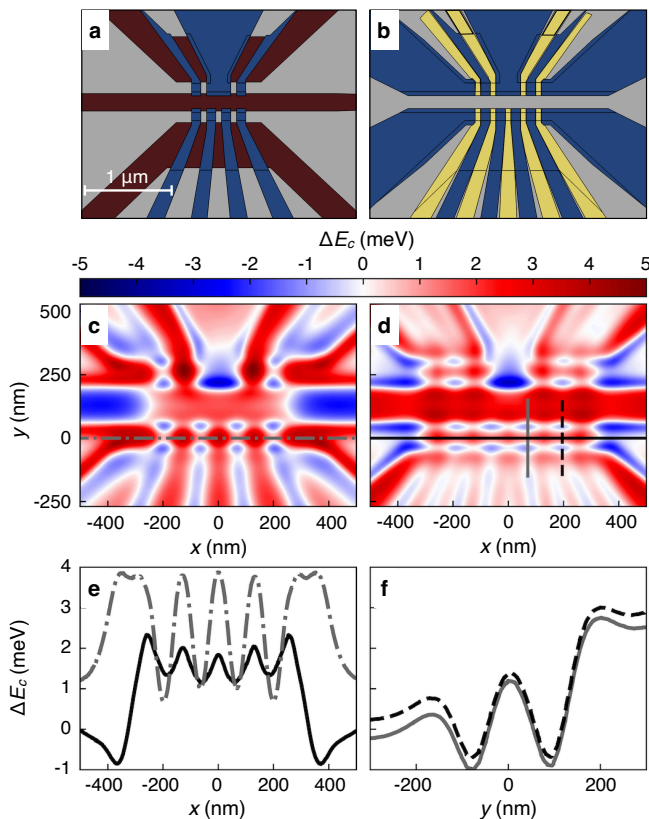


FIG. 4. Strain simulations of the quadruple-quantum-dot device of Ref. [29], for several configurations of stacked Al gates fabricated on the same heterostructure as Fig. 2. **a** Reduced gate set, including only screening gates (30 nm thick, maroon) and plunger gates (50 nm thick, blue). **b** full gate geometry, including the gate layers in **a**, as well as side-reservoir gates (shown in blue because they are formed in the same layer as the blue gates in **a**), and tunnel-barrier gates (70 nm thick, yellow). Two additional gate configurations are considered in Supplementary Fig. S2. In each case, every gate layer is covered by 2 nm of  $\text{Al}_2\text{O}_3$  (not pictured, for clarity). **c,d** Strain-induced fluctuations of  $\Delta E_c$  in the plane of the 2DEG, for the geometries shown in **a** and **b**, respectively. **e** Linecuts along the horizontal lines in **c** (dot-dashed gray curve) and **d** (solid black curve), which pass through the centers of the lower four dots. Again we highlight a primary result, that energy fluctuations in the fully covered geometry (solid black curve) are strongly suppressed compared to gates separated by gaps (dot-dashed curve). **f** Vertical linecuts indicated in **d**. Note the emergence of a strain-induced double-well potential.

either side of the dots. In the upper portion of the image, the plungers define two charge-sensing dots, surrounded by three 2DEG reservoirs. To avoid edge effects, we use a full simulation cell of size  $18 \times 18 \mu\text{m}^2$  in the  $x$ - $y$  plane and  $2 \mu\text{m}$  in the  $z$  direction. We have checked that this system size yields converged results.

To disentangle the effects of the different gate layers in our simulations, we begin with a smaller set of gates, and progressively add more gates until reaching a complete set. Figure 4 shows  $\Delta E_c$  results for the geometries shown

in panels a and b. Figure 4a includes only the screening, plunger, and upper-middle reservoir gates, while Fig. 4b includes all the gates. (Two intermediate gate sets are also considered in Supplementary Fig. S2.) The linecuts indicated in Figs. 4c and 4d are plotted in Figs. 4e and 4f. The effectiveness of gate-layer stacking is seen most clearly by comparing the horizontal lines in Figs. 4c and 4d. In Fig. 4c, this cut crosses just the four plunger gates, which are separated by gaps. In Fig. 4d, the gaps are all filled by overlapping tunnel-barrier gates, and reservoir gates are also present on either side, such that the whole cut is covered by metal. As consistent with Fig. 3, the case with gaps between the gates (dot-dashed line in Fig. 4e) has short-range oscillations of about 3 meV. Moreover, in the fully covered case (solid line), the short-range oscillations are suppressed by a factor of three. However, the oscillations have the same sign for these two geometries, in contrast with the results observed in Fig. 3d. A notable difference between these two devices is that the crossing gate in Fig. 3a covers the parallel gates *globally*, as opposed to the tunnel-barrier gates in Fig. 4b, which just fill in the gaps, locally, between the plunger gates.

The oscillation envelopes in Fig. 4e also show interesting behavior. We observe that neighboring dots can have confinement potentials of different depths, representing built-in, fixed detuning parameters on the order of 0.25-0.35 meV. Moreover, the envelopes for the two geometries have opposite curvature, which we attribute to the presence of side-reservoir gates for the full gate geometry. The different curvature signs suggest that alternative gate geometries could be used to reduce the detuning shifts, for example, by moving the side-reservoir gates further away from the dots.

Finally, we note that strain from the screening gates can have unexpected effects on quantum-dot confinement in the  $y$  direction, as demonstrated in Fig. 4f. Here, the combination of screening and plunger gates produces a double-dip feature on either side of the dot, which is weakly affected by the presence of the tunnel-barrier or reservoir gates. The peak between the dips has the opposite sign as the electrostatic dot confinement. To estimate its effect, we fit the peak to the upside-down confinement potential  $-m_t \omega_y^2 y^2 / 2$ , yielding a characteristic orbital energy of  $\hbar \omega_y \approx 1.3$  meV, where  $m_t$  is the transverse effective mass of silicon. Comparing this with typical dot orbital energies of  $\hbar \omega = 1$ -3 meV (see Supplementary Fig. S3) suggests that the strain-induced effect is not likely to produce a double-dot along  $y$ ; however, it can strongly affect the dot shape — effectively flattening and widening the bottom of the confinement potential. For weaker electrostatic confinements, the strain-induced effect will eventually dominate.

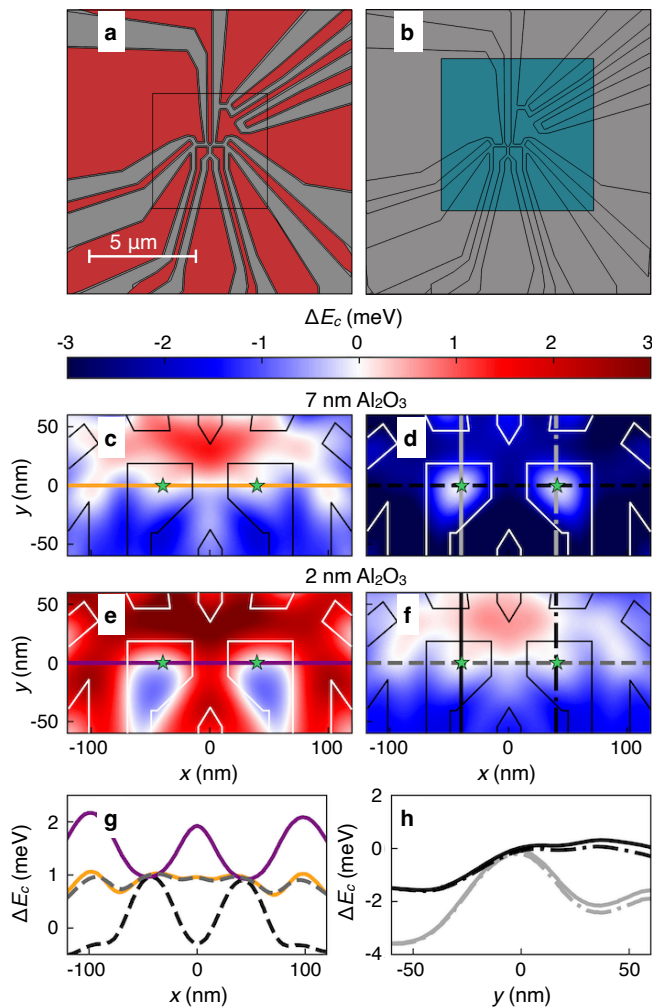


FIG. 5. Strain simulations of the two-dot device of [30], for two configurations of stacked Al gates, and two oxide thicknesses. From bottom to top, the thicknesses of the  $\text{Si}_{0.7}\text{Ge}_{0.3}$  virtual substrate, Si quantum well,  $\text{Si}_{0.7}\text{Ge}_{0.3}$  spacer, and Si cap are  $1.2\ \mu\text{m}$ , 8 nm, 30 nm, and 1 nm, respectively. **a** Reduced gate set, including only the lower layer of gates (20 nm thick), is shown in red. We also include  $\text{Al}_2\text{O}_3$  layers of variable thickness, above and below the gate layer (top layer not shown, for clarity). **b** Same as **a**, but including a global top gate (turquoise) of thickness 40 nm. **c,d** Strain-induced fluctuations of  $\Delta E_c$  in the plane of the 2DEG, for the geometries shown in **a** and **b**, respectively, where all oxide layers have a thickness of 7 nm. **e,f** Same as **c** and **d**, except the oxide layers have a thickness of 2 nm. In **c-f**, approximate dot locations are indicated by green stars, and we have shifted the energy scale such that  $\Delta E_c = 0$  at the dot centers. **g** Horizontal linecuts, indicated in panels **c-f**, with appropriate color codings. We again highlight a key result, that energy fluctuations in the covered geometry (dashed-gray curve) are strongly suppressed, but only for the case of a narrow oxide. **h** Vertical linecuts, indicated in panels **d** and **f**, with appropriate color codings.

#### D. Effect of oxide-layer thickness

In the final set of simulations, we also study gate-layer stacking, while showing how using thicker oxides modifies our main conclusions. The device we consider is based on Ref. [30], with the two variations shown in Figs. 5a and 5b. Here, the heterostructure consists of a  $1.2\ \mu\text{m}$  strain-relaxed  $\text{Si}_{0.7}\text{Ge}_{0.3}$  buffer layer, an 8 nm Si quantum well, a 30 nm  $\text{Si}_{0.7}\text{Ge}_{0.3}$  spacer, a 1 nm Si cap, a thin  $\text{Al}_2\text{O}_3$  oxide layer, a 20 nm Al metal gate, and another thin  $\text{Al}_2\text{O}_3$  layer. (We also consider the effect of an additional cobalt micromagnet layer in Supplementary Fig. S4.) To study the effects of oxide thickness, we consider two different cases: a 7 nm oxide layer (consistent with the device in [30]) and a 2 nm oxide layer (consistent with the device in [29]). This geometry is shown in Fig. 5a, while Fig. 5b also includes a 40 nm Al global gate. Results for  $\Delta E_c$  are shown in Figs. 5c-5f, for the four different combinations of oxide thicknesses and gate geometries, with corresponding linecuts shown in Figs. 5g and 5h.

We begin by confirming the effect of gate-layer stacking, by comparing Figs. 5e and 5f. For these two simulations, the oxide thickness is the same as in the previous subsections (2 nm), and the only difference in the geometries is the global top gate. The linecut in Fig. 5g with no global top gate (solid-purple curve) shows strong short-range fluctuations, with similar amplitude and shape as previous simulations, while the stacked global gate (dashed-gray curve) has strongly suppressed fluctuations. A more surprising result is observed in the dashed-black linecut, which has the same accumulation-gate geometry, but a thicker (7 nm) oxide layer. Here, the short-range oscillations have the opposite sign compared to the solid-purple curve. This behavior is reminiscent of Fig. 3e; indeed, for both cases, the stacked gates responsible for this behavior cover the plungers *globally*. Interestingly, the amplitude of the oscillations for the thick-oxide device (dashed-black curve) is strongly enhanced compared to the thin-oxide device (dashed-gray curve), as if the thicker oxide were amplifying the oscillations. We attribute this behavior to 3D aspects of the gate geometry, whose effects are difficult to predict. For completeness, we also show results for a thick oxide with no global top gate (solid-orange curve), in which the oscillations are strongly suppressed, with features coincidentally similar to the gray-dashed curve.

Finally, in Fig. 5h, we consider linecuts along the  $y$  axis that pass through the nominal centers of the quantum dots (green stars). Here, we consider only the full gate geometry, which includes the global top gate. Similar to linecuts along  $\hat{x}$ , these results confirm that stronger short-range fluctuations are obtained in the case of thicker oxides (gray curves). We also note the slight differences between results in the left- and right-hand dots in Fig. 5h (solid vs dashed curves), which are caused by long-range strain fields arising from the asymmetric top-gate configuration.

### III. DISCUSSION

We have investigated local strain fluctuations in realistic Si/SiGe quantum dot devices, arising from inhomogeneous materials layers, and in particular, from the metal top gates. For these gates, we include effects from both thermal contraction and depositional stress, finding that the former dominates for Al gates, while the latter dominates for Pd gates. Focusing on Al gates, we note that strain along the  $z$  axis ( $\varepsilon_{zz}$ ) mainly determines the variations of the conduction-band minimum ( $\Delta E_c$ ), and is strongly affected by nontrivial 3D features such as the vertical layer stacking and the gate geometry, resulting in behavior that is not always intuitive.

Despite these challenges, we can draw some general conclusions. First, we note that  $\Delta E_c$  exhibits both short-range variations that mirror the shape of the top gates, and long-range variations that produce slowly varying envelopes that modulate the fast oscillations. The amplitude of the short-range fluctuations is comparable, but often smaller, than typical electrostatic fluctuations produced by the top gates; however, unlike electrostatic fluctuations, strain-induced effects cannot be modified after fabrication. In some cases, the potential fluctuations can have a considerable effect on the shape of the dot, as in Figs. 4(g) and S3. Indeed, dot localization effects that were previously attributed to trapped charge [16–18] could potentially be explained, in full or in part, by strain effects. The long-range fluctuations cause potential shifts below neighboring plunger gates that act like built-in detuning potentials between the dots, which must be electrostatically compensated for proper gate operation.

The most important result reported in this work is that the tight stacking of gate layers provides a key tool for overcoming strain-induced potential fluctuations. Such stacked gates can be seen as largely reproducing the behavior of a uniform metal top gate. However, unexpected 3D effects can still occur, for example, when employing a thicker oxide layer between the metal gates, which can have the effect of *amplifying* the short-range potential fluctuations. Similarly, different styles of gate stacking can yield different potential profiles; for example, a globally spanning top gate (Fig. 5) is seen to cause very different behavior than local tunnel-barrier gates filling the gaps between plunger gates (Fig. 4), as evidenced by short-range oscillations with opposite signs.

In future work, as arrays of qubits are scaled up, and every aspect of qubit functionality is tightly controlled, it will be increasingly important to account for strain-induced confinement effects, which can compete with electrostatic confinement. The simplest approach to avoiding strain-induced behavior is to specifically design gate geometries to suppress these fluctuations. Clearly, gate-layer stacking is a key tool for such an approach. However, other design tools, such as modifying the lateral positions of gate electrodes, the thicknesses of oxide layers, or other 3D features of the gate geometry, could also serve this purpose. Generally, we anticipate that

strain engineering will play an important role in future qubit technologies.

### METHODS

We calculate strain profiles using the Solid Mechanics module of COMSOL Multiphysics [31]. To perform these calculations, we must specify the Young's modulus  $E$ , Poisson's ratio  $\nu$ , and coefficients of thermal expansion (CTE)  $\alpha$ , for each material. Note that each of these parameters varies with temperature, although COMSOL assumes temperature-independent values.  $E$  and  $\nu$  depend only weakly on the temperature, so we simply adopt room-temperature values for these parameters, from the COMSOL parameter library. To account for the temperature dependence of the CTEs, we define temperature-averaged CTEs as  $\bar{\alpha} = (T_i - T_f)^{-1} \int_{T_f}^{T_i} \alpha(T) dT$ , where  $T_i$  and  $T_f$  are the initial and final temperatures, respectively. We approximate these integrals using the temperature-dependent CTE data presented in Refs. [32–37]. For the SiGe alloy, we use data for Si and Ge in combination with Vegard's law to evaluate its CTE. The temperature-averaged CTEs are then given by  $\{\bar{\alpha}_{\text{Si}}, \bar{\alpha}_{\text{Si}_{0.7}\text{Ge}_{0.3}}, \bar{\alpha}_{\text{Al}}, \bar{\alpha}_{\text{Pd}}, \bar{\alpha}_{\text{Al}_2\text{O}_3}\} = \{0.76, 1.52, 14.16, 8.86, 3.30\} (\times 10^{-6} \text{ K}^{-1})$ . The biaxial strain from lattice mismatch is imposed through the initial-strain parameters  $\varepsilon_{xx} = \varepsilon_{yy} = 1.24\%$  and  $\varepsilon_{zz} = -1.01\%$ . Where specified, depositional stress in the metallic gates is imposed as an intrinsic stress. Finally, free boundary conditions [31] are enforced on every surface, except for the bottom surface, where we enforce contraction that matches the bulk thermal contraction of Si, to emulate the presence of a larger Si substrate.

The calculated strain profiles can then be related to the offsets  $\Delta E_c$  of the conduction band in the Si quantum well by the relation [19]

$$\Delta E_c = E_0 + \Xi_u \varepsilon_{zz} + \Xi_d (\varepsilon_{xx} + \varepsilon_{yy} + \varepsilon_{zz}), \quad (1)$$

where  $\Xi_u = 10.5$  eV and  $\Xi_d = 1.1$  eV are deformation potential coefficients [38], whose difference is a consequence of the anisotropy of the  $z$  valleys, which are the low-energy points of the conduction band in momentum space for the strained Si/SiGe quantum well [2]. As a result, strain effects in  $\Delta E_c$  are dominated by the  $z$  component of the strain tensor,  $\varepsilon_{zz}$ , as can be seen by comparing Figs. 2c and 2d. When computing energy fluctuations in Eq. (1), we use the strain evaluated in the 2DEG plane, which is assumed to lie 1.5 nm below the top interface of the quantum well, where the low-energy electronic wave functions of the quantum well are concentrated. Finally, unless otherwise specified,  $E_0$  is shifted in each calculation such that the asymptotic value of  $\Delta E_c$  is zero, far away from the active region containing the gates.

## ACKNOWLEDGMENTS

We are grateful to Xiao Xue, Nodar Samkharadze, Gertjan Eenink, Menno Veldhorst, and Lieven Vandersypen for sharing device designs related to this work. We also thank Hudaiba Soomro for important clarifications related to the simulations. This research was sponsored in part by the Army Research Office under Awards No. W911NF-23-1-0110, W911NF-22-1-0090, and W911NF-

17-1-0274. The views, conclusions, and recommendations contained in this document are those of the authors and are not necessarily endorsed by nor should they be interpreted as representing the official policies, either expressed or implied, of the Army Research Office or the U.S. Government. The U.S. Government is authorized to reproduce and distribute reprints for U.S. Government purposes notwithstanding any copyright notation herein.

- 
- [1] D. Loss and D. P. DiVincenzo, Quantum computation with quantum dots, *Phys. Rev. A* **57**, 120 (1998).
- [2] F. A. Zwanenburg, A. S. Dzurak, A. Morello, M. Y. Simmons, L. C. L. Hollenberg, G. Klimeck, S. Rogge, S. N. Coppersmith, and M. A. Eriksson, Silicon quantum electronics, *Rev. Mod. Phys.* **85**, 961 (2013).
- [3] G. Burkard, T. D. Ladd, A. Pan, J. M. Nichol, and J. R. Petta, Semiconductor spin qubits, *Rev. Mod. Phys.* **95**, 025003 (2023).
- [4] X. Xue, M. Russ, N. Samkharadze, B. Undseth, A. Sammak, G. Scappucci, and L. M. K. Vandersypen, Quantum logic with spin qubits crossing the surface code threshold, *Nature* **601**, 343 (2022).
- [5] A. Noiri, K. Takeda, T. Nakajima, T. Kobayashi, A. Sammak, G. Scappucci, and S. Tarucha, Fast universal quantum gate above the fault-tolerance threshold in silicon, *Nature* **601**, 338 (2022).
- [6] A. R. Mills, C. R. Guinn, M. J. Gullans, A. J. Sigillito, M. M. Feldman, E. Nielsen, and J. R. Petta, Two-qubit silicon quantum processor with operation fidelity exceeding 99%, *Science Advances* **8**, eabn5130 (2022).
- [7] A. M. J. Zwerver, T. Krähenmann, T. F. Watson, L. Lampert, H. C. George, R. Pillarisetty, S. A. Bojarski, P. Amin, S. V. Amitonov, J. M. Boter, R. Caudillo, D. Correas-Serrano, J. P. Dehollain, G. Droulers, E. M. Henry, R. Kotlyar, M. Lodari, F. Lüthi, D. J. Michalak, B. K. Mueller, S. Neyens, J. Roberts, N. Samkharadze, G. Zheng, O. K. Zietz, G. Scappucci, M. Veldhorst, L. M. K. Vandersypen, and J. S. Clarke, Qubits made by advanced semiconductor manufacturing, *Nature Electronics* **5**, 184 (2022).
- [8] M. Meyer, C. Déprez, T. R. van Abswoude, I. N. Meijer, D. Liu, C.-A. Wang, S. Karwal, S. Oosterhout, F. Borsoi, A. Sammak, N. W. Hendrickx, G. Scappucci, and M. Veldhorst, Electrical control of uniformity in quantum dot devices, *Nano Letters* **23**, 2522 (2023).
- [9] D. M. Zajac, T. M. Hazard, X. Mi, E. Nielsen, and J. R. Petta, Scalable gate architecture for a one-dimensional array of semiconductor spin qubits, *Phys. Rev. Appl.* **6**, 054013 (2016).
- [10] E. H. Chen, K. Raach, A. Pan, A. A. Kiselev, E. Acuna, J. Z. Blumoff, T. Brecht, M. D. Choi, W. Ha, D. R. Hulbert, M. P. Jura, T. E. Keating, R. Noah, B. Sun, B. J. Thomas, M. G. Borselli, C. Jackson, M. T. Rakher, and R. S. Ross, Detuning axis pulsed spectroscopy of valley-orbital states in Si/Si-Ge quantum dots, *Phys. Rev. Appl.* **15**, 044033 (2021).
- [11] B. P. Wuetz, M. P. Losert, S. Koelling, L. E. A. Stehouwer, A.-M. J. Zwerver, S. G. J. Philips, M. T. Mađzik, X. Xue, G. Zheng, M. Lodari, S. V. Amitonov, N. Samkharadze, A. Sammak, L. M. K. Vandersypen, R. Rahman, S. N. Coppersmith, O. Moutanabbir, M. Friesen, and G. Scappucci, Atomic fluctuations lifting the energy degeneracy in Si/SiGe quantum dots, *Nature Communications* **13**, 7730 (2022).
- [12] M. P. Losert, M. A. Eriksson, R. Joynt, R. Rahman, G. Scappucci, S. N. Coppersmith, and M. Friesen, Practical strategies for enhancing the valley splitting in Si/SiGe quantum wells, *Phys. Rev. B* **108**, 125405 (2023).
- [13] M. Meyer, C. Déprez, I. N. Meijer, F. K. Unseld, S. Karwal, A. Sammak, G. Scappucci, L. M. K. Vandersypen, and M. Veldhorst, Single-electron occupation in quantum dot arrays at selectable plunger gate voltage (2023), [arXiv:2309.03591](https://arxiv.org/abs/2309.03591) [cond-mat.mes-hall].
- [14] M. A. Wolfe, B. X. Coe, J. S. Edwards, T. J. Kovach, T. McJunkin, B. Harpt, D. E. Savage, M. G. Lagally, R. McDermott, M. Friesen, S. Kolkowitz, and M. A. Eriksson, Control of threshold voltages in Si/SiGe quantum devices via optical illumination (2023), [arXiv:2312.14011](https://arxiv.org/abs/2312.14011) [cond-mat.mes-hall].
- [15] L. Massai, B. Hetenyi, M. Mergenthaler, F. J. Schupp, L. Sommer, S. Paredes, S. W. Bedell, P. Harvey-Collard, G. Salis, A. Fuhrer, and N. W. Hendrickx, Impact of interface traps on charge noise, mobility and percolation density in Ge/SiGe heterostructures, [arXiv:2310.05902](https://arxiv.org/abs/2310.05902) (2023).
- [16] B. Hu and C. H. Yang, Electron spin blockade and singlet-triplet transition in a silicon single electron transistor, *Phys. Rev. B* **80**, 075310 (2009).
- [17] E. P. Nordberg, G. A. T. Eyck, H. L. Stalford, R. P. Muller, R. W. Young, K. Eng, L. A. Tracy, K. D. Childs, J. R. Wendt, R. K. Grubbs, J. Stevens, M. P. Lilly, M. A. Eriksson, and M. S. Carroll, Enhancement-mode double-top-gated metal-oxide-semiconductor nanostructures with tunable lateral geometry, *Phys. Rev. B* **80**, 115331 (2009).
- [18] B. Hu and C. H. Yang, Electron spin blockade and singlet-triplet transition in a silicon single electron transistor, *Phys. Rev. B* **80**, 075310 (2009).
- [19] T. Thorbeck and N. M. Zimmerman, Formation of strain-induced quantum dots in gated semiconductor nanostructures, *AIP Advances* **5**, 087107 (2015).
- [20] J. Park, Y. Ahn, J. A. Tilka, K. C. Sampson, D. E. Savage, J. R. Prance, C. B. Simmons, M. G. Lagally, S. N. Coppersmith, M. A. Eriksson, M. V. Holt, and P. G. Evans, Electrode-stress-induced nanoscale disorder in Si quantum electronic devices, *APL Materials* **4**, 066102 (2016).



- [21] Strain fluctuations also arise from misfit locations in plastically relaxed virtual substrates [39]; however, we do not consider such effects here.
- [22] R. M. Stein, Z. S. Barcikowski, S. J. Pookpanratana, J. M. Pomeroy, and M. D. Stewart, Alternatives to aluminum gates for silicon quantum devices: Defects and strain, *Journal of Applied Physics* **130**, 115102 (2021).
- [23] B. C. H. Mooy, K. Y. Tan, and N. S. Lai, Comparison of strain effect between aluminum and palladium gated MOS quantum dot systems, *Universe* **6**, 51 (2020).
- [24] X. Hu and S. Das Sarma, Charge-fluctuation-induced dephasing of exchange-coupled spin qubits, *Phys. Rev. Lett.* **96**, 100501 (2006).
- [25] K. Deng, F. A. Calderon-Vargas, N. J. Mayhall, and E. Barnes, Negative exchange interactions in coupled few-electron quantum dots, *Phys. Rev. B* **97**, 245301 (2018).
- [26] K. Deng and E. Barnes, Interplay of exchange and superexchange in triple quantum dots, *Phys. Rev. B* **102**, 035427 (2020).
- [27] F. Schäffler, High-mobility Si and Ge structures, *Semiconductor Science and Technology* **12**, 1515 (1997).
- [28] G. Abadias, E. Chason, J. Keckes, M. Sebastiani, G. B. Thompson, E. Barthel, G. L. Doll, C. E. Murray, C. H. Stoessel, and L. Martinu, Review article: Stress in thin films and coatings: Current status, challenges, and prospects, *Journal of Vacuum Science & Technology A: Vacuum, Surfaces, and Films* **36**, 020801 (2018).
- [29] S. F. Neyens, E. R. MacQuarrie, J. P. Dodson, J. Corrigan, N. Holman, B. Thorgrimsson, M. Palma, T. McJunkin, L. F. Edge, M. Friesen, S. N. Coppersmith, and M. A. Eriksson, Measurements of capacitive coupling within a quadruple-quantum-dot array, *Physical Review Applied* **12**, 064049 (2019).
- [30] X. Xue, B. Patra, J. P. G. van Dijk, N. Samkharadze, S. Subramanian, A. Corna, B. P. Wuetz, C. Jeon, F. Sheikh, E. Juarez-Hernandez, B. P. Esparza, H. Ramapurawala, B. Carlton, S. Ravikumar, C. Nieva, S. Kim, H.-J. Lee, A. Sammak, G. Scappucci, M. Veldhorst, F. Sebastiano, M. Babaie, S. Pellerano, E. Charbon, and L. M. K. Vandersypen, CMOS-based cryogenic control of silicon quantum circuits, *Nature* **593**, 205 (2021).
- [31] COMSOL multiphysics<sup>®</sup> v. 5.6. [www.comsol.com](http://www.comsol.com). COMSOL AB, Stockholm, Sweden.
- [32] P. Bradley and R. Radebaugh, *Properties of Selected Materials at Cryogenic Temperatures* (CRC Press, Boca Raton, FL, 2013).
- [33] N. J. Simon, *Cryogenic Properties of Inorganic Insulation Materials for ITER Magnets: A Review* (1994).
- [34] H. J. McSkimin, Measurement of elastic constants at low temperatures by means of high frequency ultrasonic waves, *The Journal of the Acoustical Society of America* **25**, 826 (1953).
- [35] M. E. Levinshtein, S. L. Rumyantsev, and M. Shur, *Properties of advanced semiconductor materials : GaN, AlN, InN, BN, SiC, SiGe* (Wiley, New York, 2001).
- [36] R. J. Corruccini and J. Gniewek, Thermal expansion of technical solids at low temperatures: A compilation from the literature (1961).
- [37] M. Burke, Thermal expansion of ceramic materials at -200° to 0° C, *Journal of the American Ceramic Society* **45**, 305 (1962).
- [38] M. V. Fischetti and S. E. Laux, Band structure, deformation potentials, and carrier mobility in strained Si, Ge, and SiGe alloys, *Journal of Applied Physics* **80**, 2234 (1996).
- [39] C. Corley-Wiciak, C. Richter, M. H. Zoellner, I. Zaitsev, C. L. Manganelli, E. Zatterin, T. U. Schüllli, A. A. Corley-Wiciak, J. Katzer, F. Reichmann, W. M. Klesse, N. W. Hendrickx, A. Sammak, M. Veldhorst, G. Scappucci, M. Virgilio, and G. Capellini, Nanoscale mapping of the 3D strain tensor in a germanium quantum well hosting a functional spin qubit device, *ACS Applied Materials & Interfaces* **15**, 3119 (2023).
- [40] M. Stopa, Quantum dot self-consistent electronic structure and the coulomb blockade, *Phys. Rev. B* **54**, 13767 (1996).
- [41] T. Barron, J. Collins, and G. White, Thermal expansion of solids at low temperatures, *Advances in Physics* **29**, 609 (1980).

## SUPPLEMENTARY INFORMATION

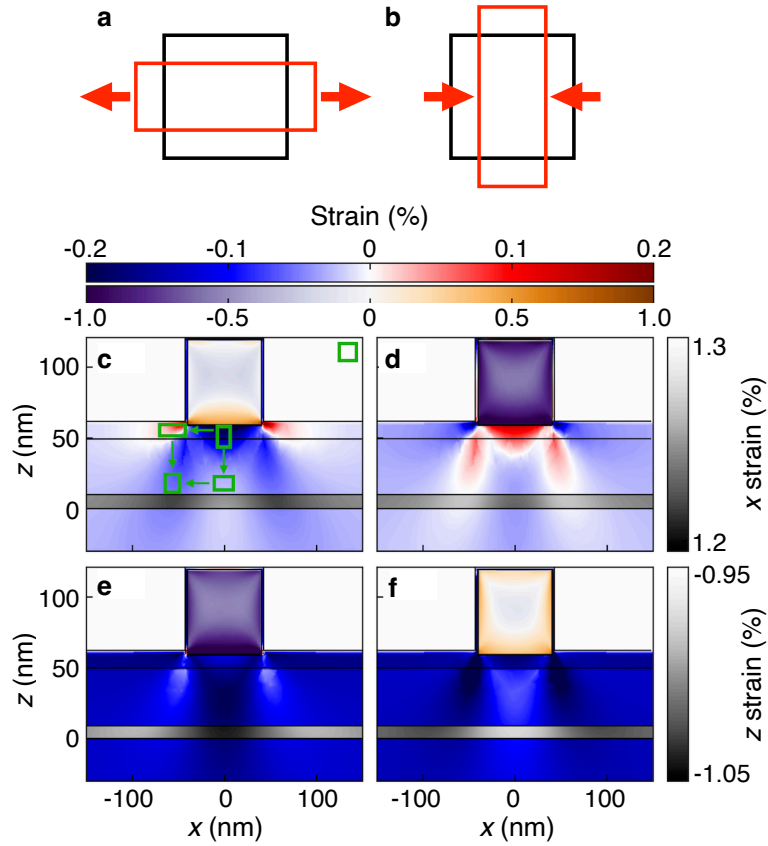


FIG. S1. Propagation of strain in a single-wire geometry. **a** In-plane tensile stress deforms an unstrained square (black) into a rectangle (red) elongated in the horizontal direction and compressed in the vertical direction. **b** In-plane compressive stress deforms the square into a rectangle compressed in the horizontal direction and elongated in the vertical direction. **c** The  $\epsilon_{xx}$  strain profile for a Pd wire with 560 MPa of depositional tensile stress. Here, three different color scales are used to show the large strain variations across multiple materials. The green boxes illustrate the propagation of strain across the SiGe and oxide layers. Compressive strain is induced directly below the wire, causing deformations similar to **b**. In turn, this induces tensile strain on either side of the wire, causing deformations similar to **a**. Similar considerations lead to the deformations shown in the lower boxes. **d** Same as **c**, except the Pd wire has 890 MPa of depositional compressive stress, causing a reversal of the strain pattern, as compared to **c**. **e**, **f**  $\epsilon_{zz}$  strain profiles, for the same conditions as **c** and **d**, respectively.

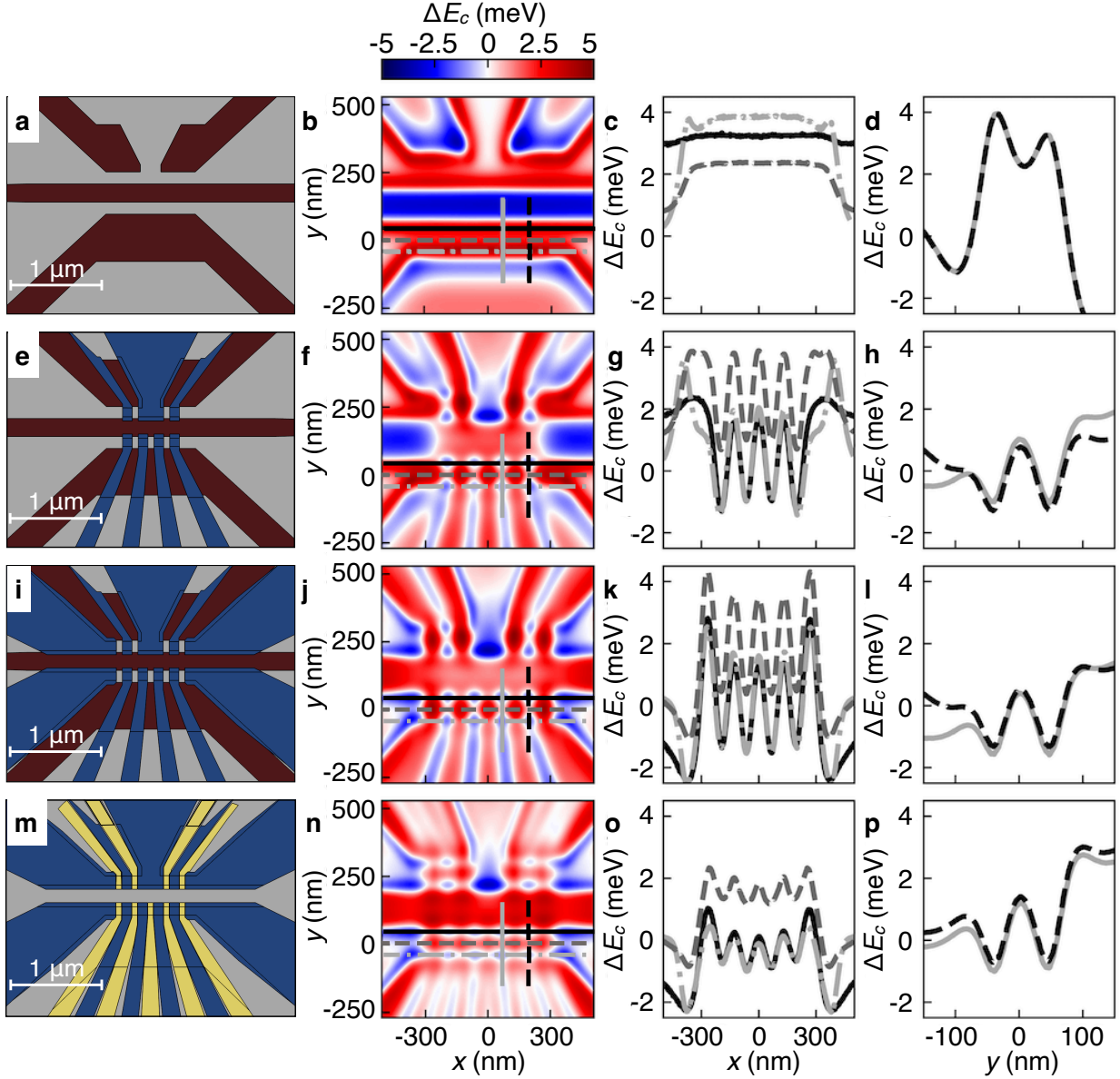


FIG. S2. Additional strain simulations of the quadruple-quantum-dot device shown in Fig. 4. The leftmost column shows the schematic gate layouts for each of the simulations. The second column shows the corresponding  $\Delta E_c$  profiles, evaluated in the 2DEG plane. The third and fourth columns show horizontal and vertical linecuts, respectively, as indicated in the second column, with matching colors and line styles. Note that the horizontal linecuts pass through the lower four dots, while the vertical linecuts run through the centers of the third and fourth dots. **a** The first gate set includes only the screening gates (maroon). **b-d** A shallow potential well forms between the screening gates, as shown in **d**, while tunnel barriers form under the edges of the gates, similar to behavior observed in Fig. 3. **e** The same gate geometry studied in Fig. 4a, which includes plunger gates and the center-reservoir gate on the top portion of the device. **f-h** Horizontal linecuts show a series of potential wells, each more than 2 meV deep. Vertical linecuts show a double-well potential, with the opposite sign as **d**, illustrating the non-trivial interactions between gate layers. **i** Same as **e**, but now including side-reservoir gates. **j-l** As expected, the reservoir gates have a subtle effect on the inner portion of the device. Comparing **g** and **k**, we see that the reservoir gates affect the long-range strain fields of the potential-well structure, causing a change of sign in the effective detuning potential between the dots. This indicates that the separation between reservoir and plunger gates, or other geometric changes in the gate design, could be used to reduce the strain-induced detuning variations between the dots. **m** The full gate geometry, also shown Fig. 4b, including the tunnel-barrier gates (yellow). Here, the  $\text{Al}_2\text{O}_3$  layer covering the screening gates is shown (gray), but the  $\text{Al}_2\text{O}_3$  layer covering the plunger gates is not shown, for clarity. **n-p** The addition of the barrier gates suppresses  $\Delta E_c$  oscillations in **o**, as seen by comparing to **k**. This illustrates the effectiveness of gate-layer stacking for reducing strain fluctuations. Note that the vertical double-well potential in **p** is only weakly affected by the final gate layer.

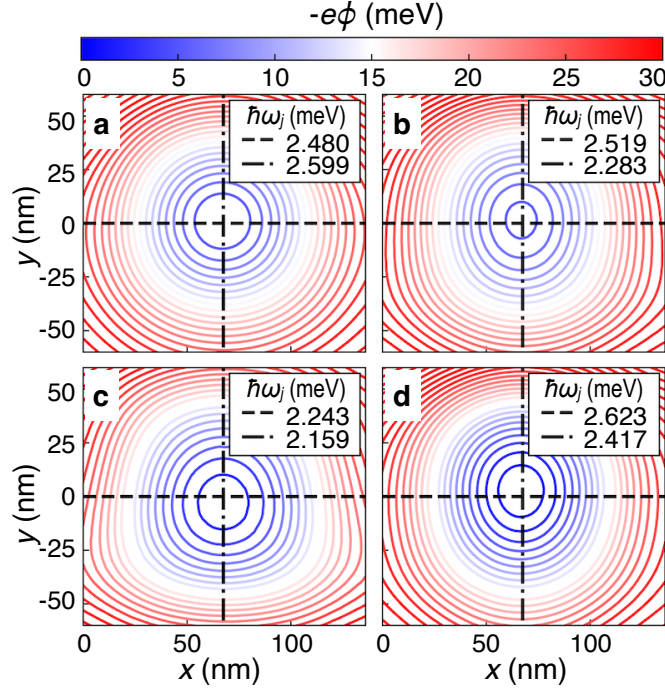


FIG. S3. Electrostatic and strain contributions to the potential-energy landscape of one of the inner dots of the device shown in Fig. 4. **a** Simulation results are shown for the electrostatic potential energy  $-e\phi$ , in the absence of strain, calculated in the Thomas-Fermi approximation [40] using COMSOL Multiphysics [31]. Here, gate voltages have been adjusted to achieve single-electron filling of the simulated dot, while depleting the other dots, and filling the nearby charge reservoirs to a density of  $2.8 \times 10^{11} \text{ cm}^{-2}$ . The resulting electrostatic profile is nearly circular, with confinement energies determined by fitting to a parabolic potential:  $\{\hbar\omega_x, \hbar\omega_y\} = \{2.480, 2.599\}$  meV. **b-d** Same as **a**, except we now include strain-induced  $\Delta E_c$  variations. Three cases are considered: **b** Al gates with 60 MPa of depositional stress, **c** Pd gates with -890 MPa of depositional stress, and **d** Pd gates with 560 MPa of depositional stress. In each case, the electrostatic contribution to the confinement potential dominates over the strain contribution, as evidenced by the small change in confinement energies compared to **a**, implying that the strain does not strongly affect dot formation. In all three cases, however, strain breaks the circular symmetry (reducing  $\hbar\omega_y$  with respect to  $\hbar\omega_x$ ), causing the dot to elongate along  $\hat{y}$ . Additionally, for dots with smaller electrostatic confinement energies (e.g.,  $\hbar\omega_{x,y} \approx 1$  meV), the strain and electrostatic potentials are comparable.

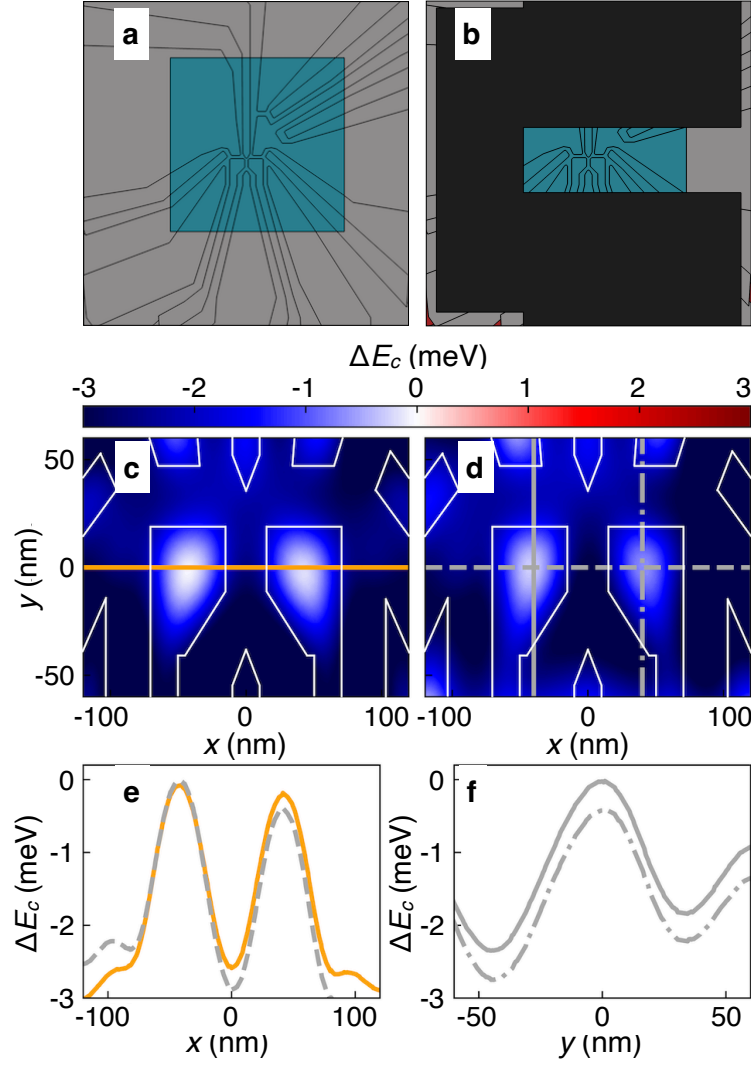


FIG. S4. Additional simulations of the device shown in Fig. 5. **a** The same gate geometry as in Fig. 5**b**. **b** Again the same device, but now including a patterned cobalt micromagnet of thickness 200 nm. The temperature-adjusted CTE value for Co, assuming a temperature drop from 293.15 K to 173 K, is given by  $12.14 \times 10^{-6} \text{ K}^{-1}$  [41]. Although we do not know the CTE corrections for lower temperatures, the trend in [41] suggests that this CTE value should give an upper bound on contraction effects. **c,d** Results for strain-induced variations of  $\Delta E_c$ , for the devices shown in **a** and **b**, respectively. **e,f** Linecuts, as indicated in **c** and **d**: **e** horizontal linecuts; **f** vertical linecuts, with matching color and line styles. We find that the relative effect of the Co is weak, and consistent with a small detuning shift.